A Parametric Shape Model Applied to Tracing the Migration of the Objects Near an Asteroid

Z. J. Yan[1]*, Y. F. Gao[1], Y. Yu[1]*†, L. Z. Shu[2], X. Y. Zeng[3], and J. Lv[1]

[1]School of Aeronautic Science and Engineering, Beihang University, Beijing, China

[2] Key Laboratory of Space Utilization, Technology and Engineering Center for Space Utilization, Chinese Academy of Sciences, Beijing, China

[3]School of Automation, Beijing Institute of Technology, Beijing 100081, China

Corresponding author: Y. Yu (yu.yang@buaa.edu.cn)

Key Points:

- A new numerical method is proposed for modeling the surface of asteroids using smooth parameter mapping.
- In this paper we present a method to model the migration of an individual object around asteroid's surface.
- We simulate the deployments of the lander on asteroid Ryugu.

Abstract

In the past decades, space missions to small bodies (Galileo, OSIRIS-REx, Hayabusa, Hayabusa2, Chang' e 2, Rosetta, etc.) have enriched us greatly with a lot of new knowledge on our solar system. In situ observations of these missions have revealed the extreme complexity and remarkable diversity of the spatial environment around their target asteroids. A study on the motion of objects in such complex environments is of great importance for understanding the evolution history of surface/sub-surface materials on the asteroids. Establishing a reasonable dynamic model is obviously the most important step. This paper proposes a method for tracking the motion of an object near the surface of an arbitrary asteroid. This method combines the irregular shape, an unlimited rotational state and asymmetric gravitational field, which are three key factors that dominate the complex movement of an object on and off the asteroid's surface. The gravitational attraction and potential are computed using the polyhedral method with corrections for the possible singularities. The asteroid's surface is then approximated using a continuous and smooth surface, and the parametric representation forms of the body are derived based on polynomial series. An event-driven scheme is designed, so that the orbital motion and surface motion are processed separately by checking the triggering events. The algorithm was implemented using C++. Benchmarking tests are organized on a local cluster, showing a satisfying performance in both accuracy and efficiency. And this method was also applied to motion control of surface detectors.

1 Introduction

The solar system small bodies have drawn increasing attention as targets for both Discovery and New Frontiers-class space missions (Van wal et al., 2017). The latest results of a series of asteroid missions have enriched our knowledge on the solar system (Li & Zeng, 2017; Hu & Xu, 2008), which will help untangle mysteries of the formation and evolution of the planets. The NEAR shoemaker mission orbited the 433 Eros for the first time on February 14, 2000, thus marking the beginning of a new era for asteroid exploration missions. Space probes can do long term in situ observations instead of simple fly-by tasks (Cheng & Santo, 1997; Farquhar et al., 2002). In-situ techniques measure surface details in a more direct way, but converting the measured flux into physical quantities often depends upon model assumptions that describe surface properties. For planning various asteroid explorations, modeling of activities is crucial to know the basic characteristics of the mission target asteroid. From September to December 2005, a variety of data were taken on the asteroid 25143 Itokawa by the Hayabusa spacecraft (Fujiwara et al., 2006); for the first time, it returned to Earth in June 2010 carrying soil samples from the asteroid (Tsuchiyama et al., 2011). To make maximum use of the abundant data to understand the origin and the evolution of the asteroids, we must send a number of spacecraft to asteroids. The JAXA Hayabusa-2 mission, combined radiometric and lightcurve inversion techniques to find the asteroid's shape, successfully arrived at the 162173 Ryugu on December 3, 2014, and is expected to return to the Earth in December 2020 (Müller et al., 2017). But challenges still remain when handing thermal data over to inversion techniques. An example of a challenge is how local structures of the asteroid influence the temperature distribution on the surface and the landing site on the target asteroid. This is also a crucial issue in the current asteroid research. Moreover, to data for most asteroids larger than about 1 km, there has been no definite evidence of the rubble-pile structure for asteroids observed by spacecraft.

It is necessary to develop new methods for simulating the surface motion of an object. This will also help us to understand better the dynamic characteristics of the spacecraft in terms of theory

and numerical simulation. Meanwhile, collisions on the surface of asteroids occur all the time (Chapman., 2004); the precise resolution modeling holds the promise for obtaining target parameters, avoiding risks, developing landing strategies in advance and providing theoretical support for the safe landing of the probe and other issues.

A continuous and smooth 3D model is key to describing the dynamic properties of spacecraft near the asteroid's surface. However, research suggests most small bodies have irregular shapes and heterogeneous constitutions (Richardson et al., 2002), which not only increases the difficulty of simulating, but also poses a great challenge in detecting collisions. Yu and Baoyin (2015) based on the division into polyhedral triangular mesh to cover the surface of asteroid, approximated with continuous quadric Bezier patches. The subpoint is recorded to track the ID of the particle throughout the process so as to analyze the dynamic behavior of the spacecraft around the asteroid's surface.

In this paper, we present a method to model the migration of an individual object around asteroid's surface. Orbital motion and surface motion are processed separately. In Section 2, we calculate the gravitational attraction and potential using the polyhedral method with a correction. Then a method for constructing a continuous and smooth surface model based on a polynomial series is introduced in Section 3. In Section 4, the complex motion routines of objects near the surface of asteroid are mainly divided into surface motion and orbital motion depending on whether the object leaves or touches the surface, where collisions are treated as instantaneous point-contact events. In Section 5, the method that we have proposed is applied to Ryugu where includes some basic tests and very detailed numerical treatments. And finally, we conclude with a brief summary in Section 6.

2 Modeling of parametric asteroid surface

In the past decades, hundreds of asteroid shape models have been derived using occultation data, thermal data, radar data, lightcurve inversion, and so on (Ďurech et al., 2015; Ostro et al., 2002). Shen & Chung (2007) presented an approach for large-scale modeling of arbitrary parametric surfaces using spherical harmonics, which has been significantly developed in computer vision, graphics, and biomedical imaging, however, there are some defects in dealing with collision problems. For this problem, they proposed a new algorithm that can be used for processing 3D closed surfaces in many different areas, called the CALD algorithm (Shen & Makedon, 2006). Wang et al. (2019) combined CALD with a polynomial series, to apply their new model with a new parameterization algorithm that makes the model applicable to general triangle meshes. Based on above analysis, we propose a new method that is suitable for arbitrary meshes of the surface and convenient for collision detection.

This paper considers a limited class of objects called starshape within the property that there exists a point in the interior of the object from which the whole object is visible (Baxansky & Kiryati., 2007).

The solution proposed in this section is to establish a one-to-one mapping between the coordinate $\mathbf{r} = (u, v, w)$ of each point on the surface of the asteroid and the unit spherical coordinates (x, y, z), parameterizing $\mathbf{r}$ with (x, y, z), so the continuous and smooth of the surface can be guaranteed.

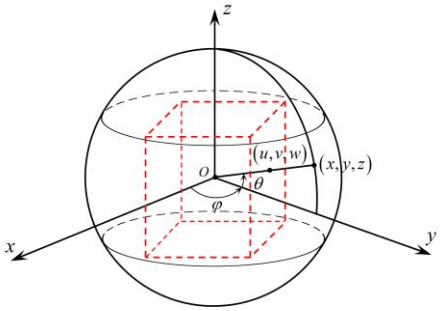

Figure 1. Center of mass along with the body-fixed frame *Oxyz*. A point of unit spherical coordinate (θ,φ) and it's Cartesian coordinate (x,y,z).

Figure 1 illustrates the center of mass along with the body-fixed frame *Oxyz*: the origin is located at the center of mass O of the asteroid, and the *x*-axis, the *y*-axis, the *z*-axis point to the three principal axes of inertia separately, which are sorted according to the magnitude of the moment of inertia to form the right-handed coordinate system as Figure 1.

A point in spherical coordinates (θ,φ) can be written at (x,y,z):

$$\begin{cases} x=\cos\theta\cos\varphi \\ y=\cos\theta\sin\varphi \\ z=\sin\theta \end{cases}. \tag{1}$$

The definition of the spherical coordinate frame is shown in Figure 1. φ is the counterclockwise angle measured from the positive x-axis in the x-y plane within the range of $[-\pi,\pi]$, and θ is the elevation angle formed between the field vector and x-y plane within the range of $\left[\frac{-\pi}{2},\frac{\pi}{2}\right]$. Equation (1) gives the transformation of spherical coordinates to Cartesian coordinates at any point on the unit sphere, which also can be used to determine (θ,φ) if (x,y,z) is given. Furthermore, all points located on the same ray as r have the same spherical coordinates, and obviously if some points have the same spherical coordinates, they are on the same ray. The surface parameterization is performed to map the sample data of the asteroid to the unit sphere data. Let r be the mapping between the coordinates of each sample point (u,v,w) and the unit sphere (θ,φ), as given by Eq. (2):

$$\mathbf{r}(\theta,\varphi)=\begin{bmatrix} u \\ v \\ z \end{bmatrix}=r(\theta,\varphi)\begin{bmatrix} \cos\theta\cos\varphi \\ \cos\theta\sin\varphi \\ \sin\theta \end{bmatrix}, \tag{2}$$

where $r(\theta,\varphi)$ is a function defined on the unit sphere. $r(\theta,\varphi)$ can be expanded into a series of polynomial series of order *N*:

$$r\left(\theta(x,y,z),\varphi(x,y,z)\right)=\sum_{k=0}^{N}\sum_{i=0}^{k}\sum_{l=0}^{i}a_{il}^{k}x^{k-i}y^{i-l}z^{l}, \tag{3}$$

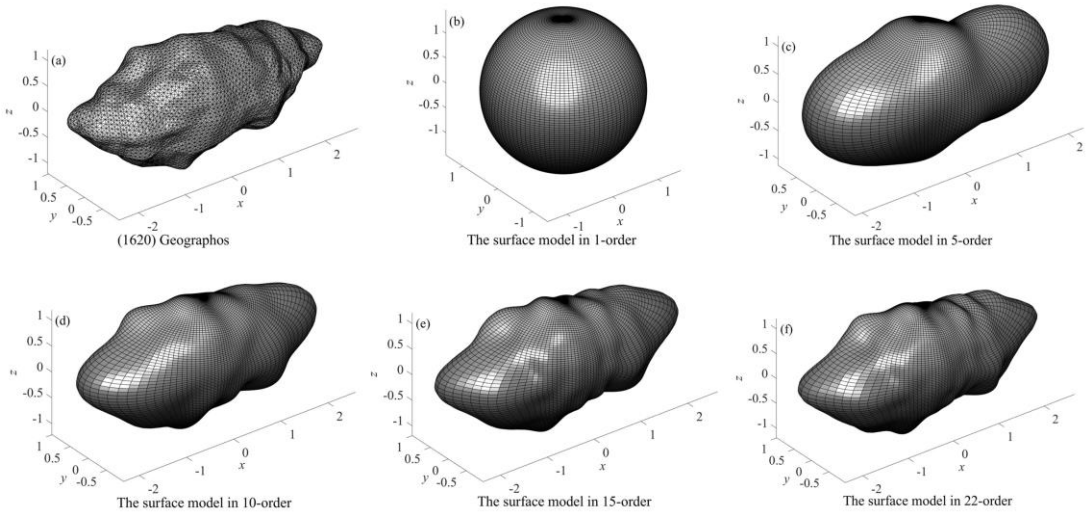

Figure 2. Asteroid (1620) Geographos, the point data, surface data and its reconstruction of polynomial series in different orders. Figure 2(a) indicates the division of triangular mesh based on 8192 vertices and 16380 faces. Figure 2(b)-2(f) indicate the surface models in 1-order, 5-order, 10-order, 15-order, 22-order of polynomial series.

where a_{il}^{k} are the expansion coefficients that we are trying to obtain. The surface model can be reconstructed with the coefficient matrix. Actually, a set of coefficients correspond to a surface description of the surface model without repetition. In general, the more coefficients we get, the higher the accuracy of the precision we realize.

The specific form of $\mathbf{r}(\theta,\varphi)$ can be derived at:

$$\mathbf{r}(x,y,z)=\begin{bmatrix}u\\v\\z\end{bmatrix}=\sum_{k=0}^{N}\sum_{i=0}^{k}\sum_{l=0}^{i}a_{il}^{k}x^{k-i}y^{i-l}z^{l}\begin{bmatrix}\cos\theta\cos\varphi\\\cos\theta\sin\varphi\\\sin\theta\end{bmatrix}, \tag{4}$$

where $\mathbf{r}(x,y,z)$ represent the sample points. (x,y,z) are the coordinates mapped from the sample point to the unit sphere.

Figure 2 indicates the original point data, the surface data of asteroid 1620 Geographos and the reconstruction of the parametric model based on polynomial series. Figure 2(a) indicates the division of triangular mesh into 8192 vertices and 16380 faces. Figure 2(b)-2(f) present the surface models in 1-order, 5-order, 10-order, 15-order and 22-order of polynomial series. Figure 2 illustrates that the higher the polynomial series order, the better the fit, and the reconstruction in 1-order is always a sphere, which means that the more coefficients we obtain, the higher the accuracy of the precision we achieve.

In conclusion, $\mathbf{r}$ can be parameterized using (x,y,z), and the parametric surface can be expressed as:

$$\boldsymbol{r}=\mathbf{r}(x,y,z)=\mathbf{S}(\theta,\varphi). \tag{5}$$

The above derivations provide sufficient geometrical information for the simulation, and they also provide a condition for the establishment of dynamic model of moving bodies near the surface of asteroids.

3 Method for Tracing the Migration

3.1 Global gravitational field

The polyhedral method has been mentioned in geology to describe the rugged surface topography of asteroids for a long time, and this methodology has further evolved and become practical with the development of digital computer technology. Werner and Scheeres (1996) proposed a polyhedron method to model the exterior gravitational field near asteroids of unusual shapes. This is one of the most typical methods used to describe the global gravitational field of an asteroid. And two types of singularity problems in the global field range are separately corrected by Tsoulis and Petrovic (2001), Yu and Baoyin (2015). Using the results, it becomes possible to compute the global gravitational field using Eqs. (6)-(7).

$$U = \frac{1}{2} G\sigma \left(\sum_{e \in ES} \boldsymbol{r}_e \cdot P_e(\boldsymbol{r}) - \sum_{f \in FS} \boldsymbol{r}_f \cdot Q_f(\boldsymbol{r}) \right), \tag{6}$$

$$\nabla U = -G\sigma \left(\sum_{e \in ES} P_e(\boldsymbol{r}) - \sum_{f \in FS} Q_f(\boldsymbol{r}) \right). \tag{7}$$

Eqs. (6)-(7) provide the close forms of polyhedral attraction and its potential, where G is the gravitational constant, σ is the bulk density, ES and FS represent the sets of all edges and faces of the polyhedron respectively, $\boldsymbol{r}_e$ and $\boldsymbol{r}_f$ are vectors from the field point to the polyhedral points on edge e and face f respectively. $P_e(\boldsymbol{r})$ and $Q_f(\boldsymbol{r})$ are defined as:

$$P_e(\boldsymbol{r}) = \begin{cases} 0 & \boldsymbol{r} \in e \\ L_e^f \mathbf{E}_e \cdot \boldsymbol{r}_e & \boldsymbol{r} \notin e \end{cases}, \tag{8}$$

$$Q_e(\boldsymbol{r}) = \begin{cases} 0 & \boldsymbol{r} \in \overline{f} \\ \omega_f \mathbf{F}_f \cdot \boldsymbol{r}_f & \boldsymbol{r} \notin \overline{f} \end{cases}, \tag{9}$$

where $\boldsymbol{r}$ is the field point vector, L_e^f is the line integral associated with the edge e of the face f, ω_f is the solid angle, $\mathbf{E}_e$ and $\mathbf{F}_{\mathrm{f}}$ are constant edge dyad and face dyad separately, and the points causing the singularity are confined to the sides of surface f , that we denoted $\overline{f}$.

Eqs. (6)-(7) provide formulas for polyhedral gravity and potential, which can be applied at any field points on the surface, inside and outside of the polyhedron.

3.2 Orbital motion

Only the gravity of the asteroid on the object is considered to simulate the motion of the spacecraft or some objects near the asteroid. A complete form of orbital equations of a unit massive object around asteroid in the body-fixed Cartesian frame has been presented by Scheeres et al. (1998), which describes an autonomous system:

$$\ddot{\boldsymbol{r}}+2\boldsymbol{\omega}\times\dot{\boldsymbol{r}}+\boldsymbol{\omega}\times\left(\boldsymbol{\omega}\times\boldsymbol{r}\right)+\boldsymbol{\alpha}\times\boldsymbol{r}=-\nabla U\,, \tag{10}$$

where $\boldsymbol{\omega}$ and $\boldsymbol{\alpha}$ are the angular velocity vector and angular acceleration vector respectively. In particular, by considering the rotation state of the fixed-axis in the asteroids (most of the asteroids observed are in such a rotation state) (Pravec et al., 2002), which can be regarded as being in a permanent Euler's rotation state, we can study the short-term orbits. Let $\boldsymbol{\alpha}=0$, from the Eq. (10) we have:

$$\ddot{\boldsymbol{r}}+2\boldsymbol{\omega}\times\dot{\boldsymbol{r}}+\boldsymbol{\omega}\times\left(\boldsymbol{\omega}\times\boldsymbol{r}\right)=-\nabla U\,. \tag{11}$$

Next, we introduce the definition of effective potential:

$$V=-\frac{1}{2}\left(\boldsymbol{\omega}\times\boldsymbol{r}\right)\cdot\left(\boldsymbol{\omega}\times\boldsymbol{r}\right)+U\,. \tag{12}$$

We obtained:

$$\ddot{\boldsymbol{r}}+2\boldsymbol{\omega}\times\dot{\boldsymbol{r}}=-\nabla V\,, \tag{13}$$

where Eq. (13) describes the orbital motion of a moving body in the field rotating around the asteroid.

3.3 Surface motion

The object's travel in the curved surface can be approximated by the motion in the parametric surface in our method. The forces on the object include: gravity, centrifugal force of rotation, Coriolis force, support force perpendicular to the surface and friction tangent to the surface in the case of body-fixed frame. In this section, the focus is on how the lander settles or moves on the parametric surface of asteroid. Specifically, this paper focuses on the ideal case of bouncing, and sliding, while the real situation is more complex. Because the gravity of an asteroid is extremely low, it means that bounces on a hard surface become more elastic than expected (Tardivel et al., 2014), therefore, the rigid contact force is the simplified form, and Coulomb friction is applied to the object model. At any position of the surface, the kinetic equation of the object is given (Yu & Baoyin, 2015):

$$\ddot{\boldsymbol{r}}+2\boldsymbol{\omega}\times\dot{\boldsymbol{r}}=-\nabla V+N\hat{\boldsymbol{n}}-\mu_k N\hat{\dot{\boldsymbol{r}}}\,, \tag{14}$$

where N is the amplitude of the normal supportive force, $\hat{\boldsymbol{n}}$ is the unit normal vector of the surface pointing out of the asteroid body, and μ_k is the coefficient of dynamic friction. Next, we define a unit local affine frame $\left(\hat{\boldsymbol{e}}_\theta,\hat{\boldsymbol{e}}_\varphi,\hat{\boldsymbol{n}}\right)$ on the surface at spherical coordinates $\left(\theta,\varphi\right)$ as shown in Figure 3, according to Eq. (9), it yields:

$$\hat{\boldsymbol{e}}_\theta=\frac{\mathbf{S}_\theta}{\left|\mathbf{S}_\theta\right|},\ \hat{\boldsymbol{e}}_\varphi=\frac{\mathbf{S}_\varphi}{\left|\mathbf{S}_\varphi\right|},\ \hat{\boldsymbol{n}}=\frac{\hat{\boldsymbol{e}}_\theta\times\hat{\boldsymbol{e}}_\varphi}{\left|\hat{\boldsymbol{e}}_\theta\times\hat{\boldsymbol{e}}_\varphi\right|}\,. \tag{15}$$

Note that $\mathbf{S}_\theta$ and $\mathbf{S}_\varphi$ represent the partial derivative of Eq. (9) versus θ and φ respectively. $\hat{\boldsymbol{e}}_\theta$ and $\hat{\boldsymbol{e}}_\varphi$ determine the tangent plane at $\left(\theta,\varphi\right)$, since the object moves within the surface, the velocity vector $\dot{\boldsymbol{r}}$ lies on the tangent plane. Then the first-order and second-order time derivative of Eq. (9) yield Eq. (16) and Eq. (17):

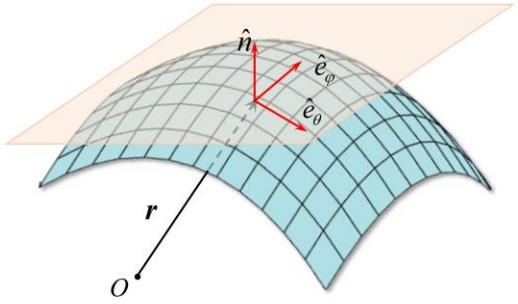

Figure 3. The unit local affine frame on the surface of parametric surface. The origin locates at the position of the object and three axis vectors point to $\hat{\boldsymbol{e}}_\theta$, $\hat{\boldsymbol{e}}_\varphi$ and $\hat{\boldsymbol{n}}$. The light salmon-colored plane indicates the tangent plane of surface at the object position, and the dark cyan surface

indicates the parametric surface.

$$\dot{\boldsymbol{r}} = \mathbf{S}_\theta \dot{\theta} + \mathbf{S}_\varphi \dot{\varphi}, \tag{16}$$

$$\ddot{\boldsymbol{r}} = \mathbf{S}_\theta \ddot{\theta} + \mathbf{S}_\varphi \ddot{\varphi} + \mathbf{S}_{\vartheta\theta} \dot{\theta}^2 + 2\mathbf{S}_{\theta\varphi} \dot{\theta}\dot{\varphi} + \mathbf{S}_{\varphi\varphi} \dot{\varphi}^2, \tag{17}$$

where $\mathbf{S}_{\theta\theta}$, $\mathbf{S}_{\varphi\varphi}$ and $\mathbf{S}_{\theta\varphi}$ are the second-order partial derivatives vectors of Eq. (9).

Substituting Eq. (5), Eq. (16), Eq. (17) into Eq. (14) yields:

$$\mathbf{S}_\theta \ddot{\theta} + \mathbf{S}_\varphi \ddot{\varphi} = N\hat{\boldsymbol{n}} - \mathbf{F}, \tag{18}$$

$$\mathbf{F} = \nabla V \circ B + \mu_k N \frac{\mathbf{S}_\theta \dot{\theta} + \mathbf{S}_\varphi \dot{\varphi}}{\left| \mathbf{S}_\theta \dot{\theta} + \mathbf{S}_\varphi \dot{\varphi} \right|} + 2\boldsymbol{\omega} \times \left(\mathbf{S}_\theta \dot{\theta} + \mathbf{S}_\varphi \dot{\varphi} \right) + \mathbf{S}_{\theta\theta} \dot{\theta}^2 + 2\mathbf{S}_{\theta\varphi} \dot{\theta}\dot{\varphi} + \mathbf{S}_{\varphi\varphi} \dot{\varphi}^2, \tag{19}$$

where $\circ$ represents the composition of functions. Note that $\mathbf{S}_\theta \cdot \hat{\boldsymbol{n}} = 0$ and $\mathbf{S}_\varphi \cdot \hat{\boldsymbol{n}} = 0$, so taking the dot product of Eq. (18) with S_θ and S_φ, we obtain:

$$\begin{bmatrix} \mathbf{S}_\theta \cdot \mathbf{S}_\theta & \mathbf{S}_\theta \cdot \mathbf{S}_\varphi \\ \mathbf{S}_\varphi \cdot \mathbf{S}_\theta & \mathbf{S}_\varphi \cdot \mathbf{S}_\varphi \end{bmatrix} \begin{bmatrix} \ddot{\theta} \\ \ddot{\varphi} \end{bmatrix} = - \begin{bmatrix} \mathbf{S}_\theta \cdot \mathbf{F} \\ \mathbf{S}_\varphi \cdot \mathbf{F} \end{bmatrix}. \tag{20}$$

The coefficient matrix of this two-dimensional system is always nonsingular because $\mathbf{S}_\theta$ and $\mathbf{S}_\varphi$ are independent, which determines the solution to Eq. (20) is always unique, while the differential equation of the unit mass point motion on the parametric surface is given by Eq. (20).

Combining Eq. (18) and Eq. (19), we have

$$N = \hat{\boldsymbol{n}} \cdot \mathbf{F}, \tag{21}$$

where Eq. (21) gives the expression of the supporting force *N*. It should be noted that the normal supporting force needs to be calculated at each step, since the constraint condition is unilateral, and the motion is valid only if *N* is positive.

3.4 Event-driven modelling of free movement near the surface

The dynamic equations of the orbital motion and surface motion of the object around the asteroid have been given in Eq. (13) and Eq. (20). Actually, the motion near the surface of the asteroid mixes various routines, such as lift-off, bouncing, slipping, or a combination of this series of comp-

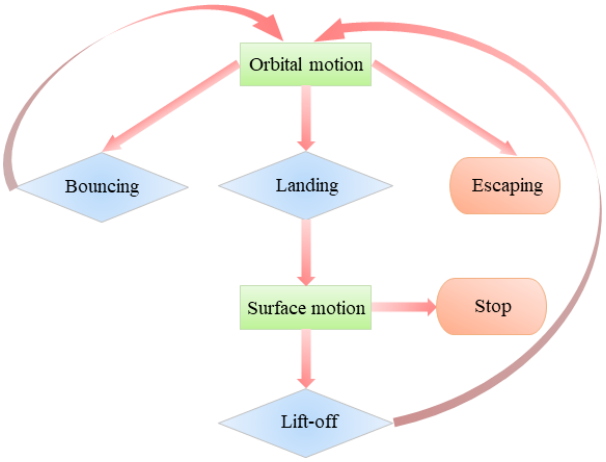

Figure 4. Event-driven model of free motion of an object near the surface of asteroid. Rectangles represent process states, rounded rectangles represent terminate states, and diamond boxes represent events.

lex movements. Based on our model, only the orbital motion and the surface motion are distinguishable, other motions can be achieved through the conversion between these two modes. What triggers the transformation is some events that may have occurred during the motion. Therefore, we propose a model called the event-driven model, which is an appropriate method to establish the free motion model of the object near the surface around the asteroid, as illustrated in Figure 4. These events are discussed in detail below.

3.4.1 Orbital motion event

Two events can be triggered in orbital motion: bouncing and landing (see Figure 5). Collision detection is performed first to deal with these two kinds of events. The most important thing is to determine whether the object enters into the surface of asteroid. For any two adjacent time steps t_k and $t_{k+1}\left(k=0,1,2,\ldots\right)$ in the numerical integration, the relative position vectors are denoted as $\boldsymbol{r_k}\left(x'_k,y'_k,z'_k\right)$ and $\boldsymbol{r_{k+1}}\left(x'_{k+1},y'_{k+1},z'_{k+1}\right)$ respectively, which can be represented by $\left(r,\theta,\varphi\right)$:

$$\begin{cases} x' = r\cos\theta\cos\varphi \\ y' = r\cos\theta\sin\varphi \\ z' = r\sin\theta \end{cases}. \tag{22}$$

$r=\left|x'^2+y'^2+z'^2\right|$, the position vector corresponds to a unique unit spherical coordinate $\left(\theta,\varphi\right)$, which we have described in Section 3. From Eq. (9), the surface can be expressed as $\mathbf{S}\left(\theta\left(x,y,z\right),\ \varphi\left(x,y,z\right)\right)$ with parameters $\left(\theta,\varphi\right)$. Where $\left(x,y,z\right)$ are the Cartesian coordinates which can be represented as Eq. (23):

$$\begin{cases} x = \cos\theta\cos\varphi \\ y = \cos\theta\sin\varphi \\ z = \sin\theta \end{cases}. \tag{23}$$

A collision with the surface occurs when:

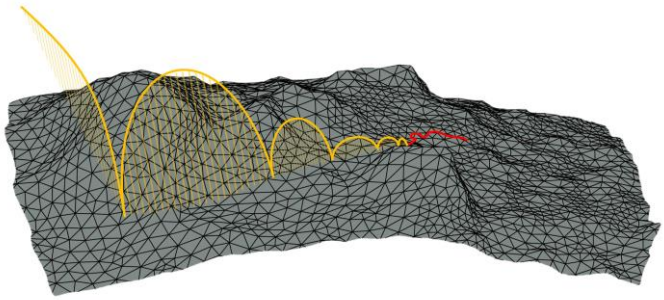

Figure 5. Bouncing and landing events of orbital motion near the surface. The yellow line indicates the orbital trajectory and the red line indicates the surface trajectory.

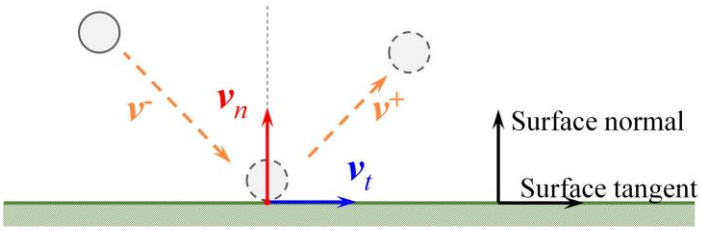

Figure 6. Change in velocity before and after the collision.

$$|\boldsymbol{r_k}| > |\mathbf{S}(\theta_k, \varphi_k)| \cap |\boldsymbol{r}_{k+1}| \le |\mathbf{S}(\theta_{k+1}, \varphi_{k+1})|. \tag{24}$$

A local linear approximation is used to determine the location r_c and velocity $\boldsymbol{v}_c^-$ of the collision since the time step is really tiny:

$$\boldsymbol{r}_c = (1-\lambda_1)\boldsymbol{r_k} + \lambda_1 \boldsymbol{r}_{k+1}, \tag{25}$$

$$\boldsymbol{v}_c^- = \lambda_2 \dot{\boldsymbol{r}}_k + (1-\lambda_2)\dot{\boldsymbol{r}}_{k+1}, \tag{26}$$

$$\lambda_1 = \frac{\left(|\boldsymbol{r_k}| - |\mathbf{S}(\theta_k, \varphi_k)|\right)|\boldsymbol{r}_{k+1}|}{|\boldsymbol{r_k}||\mathbf{S}(\theta_{k+1}, \varphi_{k+1})| - |\boldsymbol{r}_{k+1}||\mathbf{S}(\theta_k, \varphi_k)|}, \tag{27}$$

$$\lambda_2 = \frac{\left(|\boldsymbol{r_k}| - |\mathbf{S}(\theta_k, \varphi_k)|\right)|\mathbf{S}(\theta_{k+1}, \varphi_{k+1})|}{|\boldsymbol{r_k}||\mathbf{S}(\theta_{k+1}, \varphi_{k+1})| - |\boldsymbol{r}_{k+1}||\mathbf{S}(\theta_k, \varphi_k)|}. \tag{28}$$

When the classical collision theory is adopted, the collisions are treated as instantaneous events. In the case of spacecraft or gravel, the impact of the collision on the motion of asteroid can be ignored, since the time is tiny for the action, and only the impact of contact force on the surface to state of object is considered. We have that the position $\boldsymbol{r_c}$ remains unchanged before and after the collision, and the relative velocity changes from $\boldsymbol{v}^-$ to $\boldsymbol{v}^+$ (figure 6).

Suppose that the collision occurs at the tangent plane of the smooth surface at $\boldsymbol{r_c}$. The normal and tangential restitution are parameterized by the coefficient $\varepsilon_n \left(0 \le \varepsilon_n \le 1\right)$ and $\varepsilon_t \left(0 \le \varepsilon_t \le 1\right)$

respectively, and the normal and tangent components of the incoming and outgoing velocities during collision can be represented as:

$$\boldsymbol{v}^- = \boldsymbol{v}_n^- + \boldsymbol{v}_t^-, \tag{29}$$

$$\boldsymbol{v}^+ = -\varepsilon_n \boldsymbol{v}_n^- + \varepsilon_t \boldsymbol{v}_t^- . \tag{30}$$

In Eq. (29) and Eq. (30), the normal component of the velocity reverses, and the tangent component of the velocity maintains the same direction during collision, and the magnitude changes, which is illustrated in Figure 5. For example, ε_n=0 , ε_t=0 means completely inelastic collisions, after which, the velocity becomes 0; ε_n=1 , ε_t=1 means that the tangential component of velocity reverses.

Calculating the next jump height according to the magnitude of normal velocity $\left|\boldsymbol{v}_n^+\right|$ and the local normal gravity acceleration g_n , here we define the resolution of distance for numerical simulation:

$$l = \frac{\left|\boldsymbol{v}_n^+\right|^2}{2 g_n L}, \tag{31}$$

where L is the equivalent radius of the asteroid, which is same to the radius of a sphere of the equivalent volume. We denote l_ε as quantities less than 10^{-4} in calculation. The object bounces from the surface when $l > l_\varepsilon$, and enters orbital motion in the next time step. The orbital motion terminates when the object escapes beyond the range of the gravity of the asteroid. (Where we take the Hill radius of the asteroid as the boundary (Hamilton & Burns, 1992).)

3.4.2 Event-driven modelling of free movement near the surface

There is a type of event that can be triggered by surface motion: lift-off (Figure 7). When the object slides on the surface of the asteroid and exceeds the speed of lift-off, it will leave the surface and enter orbit, referred to as the lift-off (Van wal et al., 2016, 2017).

As we mentioned in Section 4.2, only when the support force N is positive, the motion is effective of the object on the surface, otherwise, the object will leave the surface. The switch between these two modes is triggered primarily when the sign of the normal contact force alternates, thus the lift-off can be judged by detecting the sign of the normal contact force. Further, the initial position and the initial velocity of the next orbital motion can be determined according to Eq. (17) and Eq. (24).

The orbital motion terminates when the relative velocity is 0 and the instantaneous velocity will not exceed the limitation of the static friction force, therefore it follows from Eq. (14) and Eq. (21) that:

$$\mu_s \left|\nabla V \cdot \hat{\boldsymbol{n}}\right| > \left|\left(\nabla V \cdot \hat{\boldsymbol{n}}\right)\hat{\boldsymbol{n}} - \nabla V\right| . \tag{32}$$

4 An application to 162173 Ryugu

By integrating the derivation mentioned above, we implemented a simulation platform using C++, Matlab, Fortran for tracking the motion of objects near the surface of an asteroid. A series of benchmarking tests are given to test the performance of the methodology proposed in this paper. The asteroid 162173 Ryugu is considered because it has attracted extensive attention from the whole world as the target of Hayabusa2 mission in recent years, it is planned to return materiel

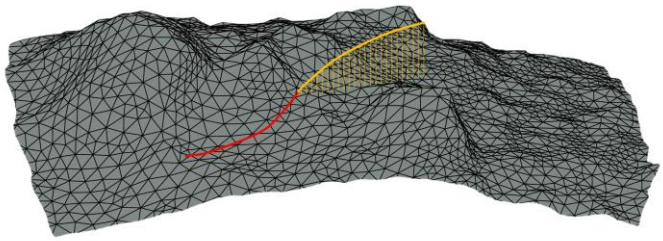

Figure 7. The lift-off event of surface motion in the surface. The yellow line indicates the orbital trajectory and the red line indicates the surface trajectory.

from the asteroid to Earth by 2020, and scientists are expected to find some information about the origin of the solar system. We have parameterized the surface of 162173 Ryugu and performed several simulations about the motion of objects near the surface of the asteroid.

4.1 Typical descending trajectories

Using the collision simulator, the orbital dynamics simulator, and the contact dynamics simulator, implementing the parametric model of bounces, landing and lift-off, the migration of the objects near an asteroid can be traced. The early observations and the spacecraft have mapped the entire surface of Ryugu with sufficient resolution to see details, and suggest that there are large boulders in the surface. And it is even more amazing that Ryugu was almost spherical, it's very different from most of the asteroids we have found (Müller et al., 2017). The Japanese probe Hayabusa2 visited Ryugu in 2018, and a small tantalum projectile was fired into the surface to collect the cloud of surface debris (Watanabe et al., 2019). JAXA planned to collect samples in around October 2018, however, it found that the surface of the Ryugu was too rugged to land, so they had to make a tremendous effort to redeploy the landing site. These are worthy of our in-depth exploration.

We adopt a parametric model of asteroid Ryugu expressed by polynomial series in 22-order, and we assume the coefficients are all constants for asteroid Ryugu in this model. Hypothetically, the bulk density 1.19 g/cc, and the period 7.627h, the dynamic friction coefficient $\mu_k = 5$ and the static friction coefficient $\mu_s = 6$. It has been established that the most solar system asteroids are the result of continual impacts, and are enveloped by regolith. Later in the evolution, larger craters saturate the surface (Housen et al., 1979, 1982), making the surface of asteroids extremely rugged, so here we choose a larger friction coefficient to optimize the simulation as much as possible. And the spacecraft Hayabusa bounced with a coefficient of restitution of 0.83 on Itokawa (Tardivel et al., 2014), we choose the normal restitution coefficient $\varepsilon_n = 0.8$ and the tangent restitution coefficient $\varepsilon_t = 0.8$. Figure 8 shows five typical trajectories that simulate the descent of lander released by detector. Trajectory 1 to 4 initialized at the same position with different velocities. Trajectory 1 indicates the free-fall motion, the object experienced a conversion from orbital motion to surface motion, and stopped on the surface after several

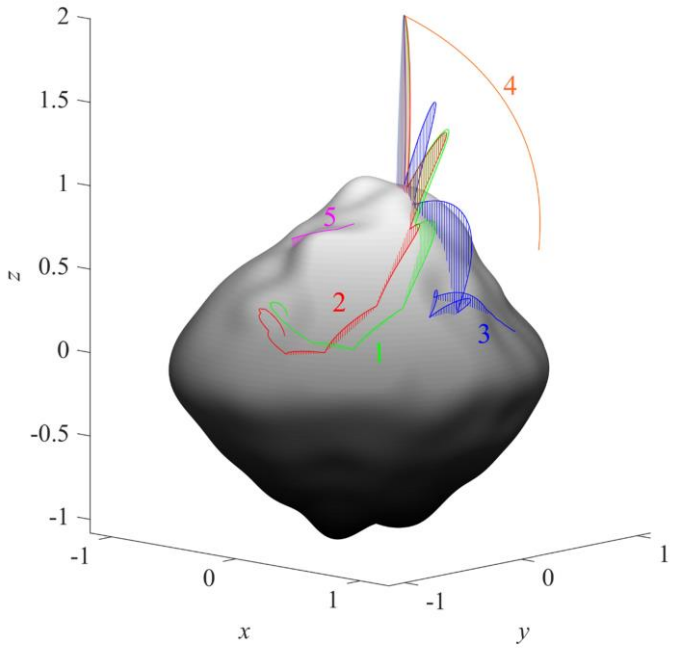

Figure 8. The model of asteroid Ryugu and the trajectories marked with different colors indicate the typical motion patterns.

collisions. Trajectory 2 and trajectory 3 have similar initial velocities but went through completely different paths, and the differentiation is severe, that means the surface of Ryugu is extremely rugged, orbital motion and surface motion are always unstable, even a tiny change in the initial conditions can make the landing site completely different, therefore it is critical to explore the detector landing on the asteroid's surface. Trajectory 4 indicates the escaping motion. When the velocity exceeds the escaping velocity, the object deviates from the asteroid. Trajectory 5 indicates the lift-off, a pattern may occur after the release. When the sliding speed exceeds the separating speed, the object will lift off the surface and converted from surface motion to orbital motion.

4.2 Analysis of landing mechanics near Ryugu

In this section, we simulated the fixed-point landings issues of the object, and several results will be analyzed, especially the initial velocity, release range of the initial position, and the range of final landing site. In general, the object should be released near the saddle points of the amended potential, where the points have low energy, and the initial velocity is always directed along a specific favorable direction (Tardivel et al., 2014). In this work, we pay more attention to the propagation properties of release error than the flying dynamics. I. e., we randomly select a fixed initial position, with the velocity directed along the radial direction to the inside, and a crater carved by the impact will be a targeted landing site. The initial position is located at longitude -82.8° and latitude 54°, an elevation of 60 meters, we choose this height because it is close to the level of rovers released by Hayabusa2.

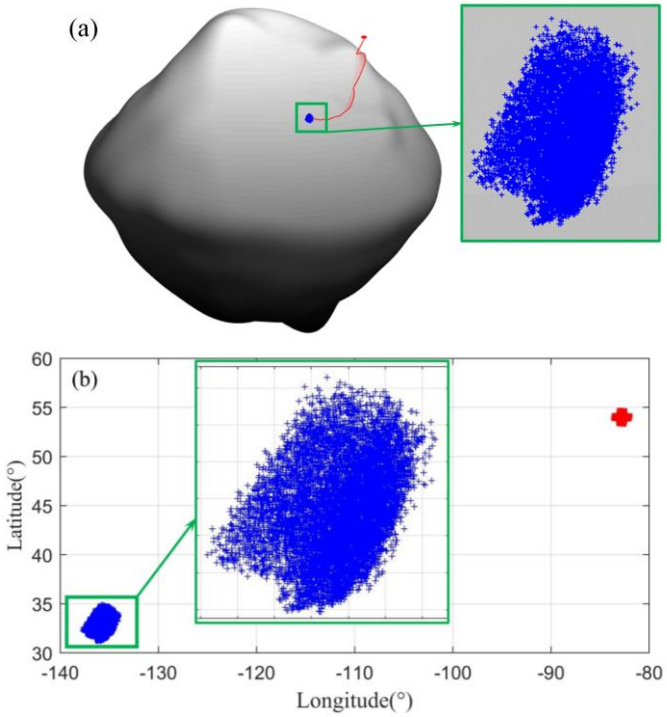

Figure 9. (a) indicates the simulation of a deployment on Ryugu. The red cloud indicates the objects with an initial position of 25 m^2, the blue cloud indicates the final landing site, and the red line indicates one arbitrary trajectory. (b) A longitude/latitude map of the initial positions and the final positions.

Figure 9(a) shows the deployment within 25 m^2 of the initial position. The release position of the object is arbitrarily selected to fall within the radius of the release point of 2.5 m, and the initial velocity is zero. Figure 9(b) shows a map of the initial and the final positions. The red cloud indicates the initial positions, the blue cloud of crosses on the Ryugu represents the final resting positions, and one of these trajectories is shown with a red line. We found that the final positions are high concentrated, we can find most of these points in a very concentrated area, which may reveal that the final position of the object is a position of relatively low energy. According to our surface model, we found this to be the case.

In Figure 10, we compare the change of the resting position of the object with the same initial velocity zero but with different initial positions. We found that when the radius range of released objects is expanded into 5 m, the final positions are a little scattered, but there still remains part of concentration. When the release radius of the initial position is extended to 7 m, the final resting position is more dispersed, which coincides with the concentration point of the initial re lease position with a radius of 2.5 m and 5 m, and none of the test points escape. Due to the instability of surface motion and orbital motion, the position of the resting point of the object is very sensitive to the initial conditions.

Figure 11 shows the longitude and latitude map of the final positions of the test points with different velocities. The red crosses represent the points with velocity of 0 m/s, the blue crosses represent the points with velocity of 1 m/s, and the green crosses represent the velocity of 1.5 m/s. The final position spread out more and more as the initial release velocity increases,

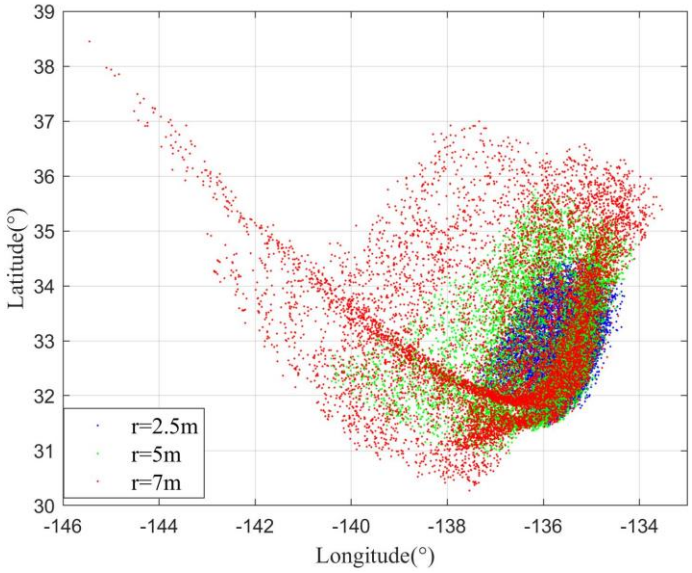

Figure 10. Longitude and latitude map of the final positions with differert ranges of initial posiiton.

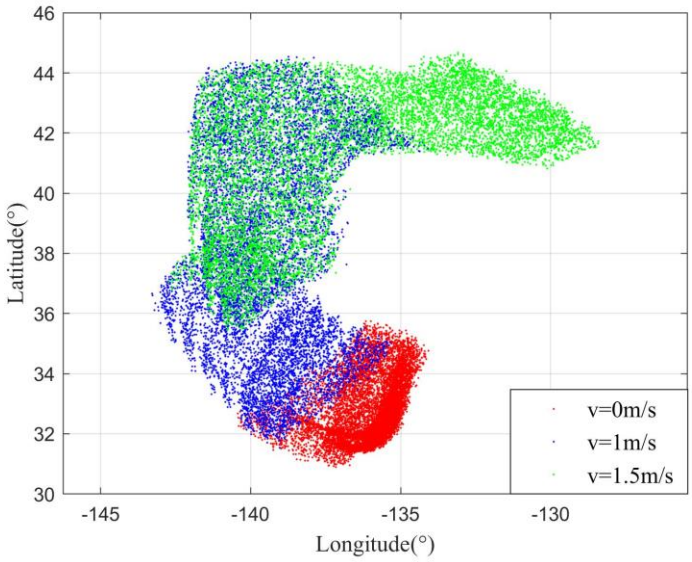

Figure 11. Longitude and latitude map of the final positions with different velocities.

nevertheless, compared to the sensitivity of the final positions to the initial position, the final position is still predictable with different velocities. And in the surface model that we have reconstructed in parametric form, it was found that the region where the most test points resided was always a flat area with low slope. Because this paper's focus is the rationality and feasibility of our surface model and to provide a relatively effective landing scheme in Ryugu, it will not expand unnecessarily the surface properties of the asteroid. In the above simulation, in the final positions of the test points were relatively concentrated within a release radius of 2.5 m in free-fall

motion. The initial positions where objects are released are stochastic, and a similar simulation could be performed for more specific research.

Moreover, we found that the trajectories rested after a few impacts, and the time to terminate was mostly around 1.8 h. No trajectories were found to survive an extremely long time orbiting around the target. It could be because only the free-fall motion of objects from the elevation 60 m is considered, the trajectories are very limited, when the elevation changes and the speed is nonzero, the final result is completely different. The simulations have confirmed the feasibility of our methodology.

5 Conclusions

This paper is devoted to tracing the migration of objects on and near the surface of asteroids. We propose a new numerical method for modeling the surface of asteroids using smooth parameter mapping. The polynomial series is used to establish the model of a continuous and smooth surface. And an event-driven method is developed for collision detection that implemented transition between orbital motion and surface motion. The validity of the parametric method is verified by comparing the original data that we have obtained and the reconstructed model of asteroid (1620) Geographos. Numerical simulations were performed to reconstruct descending trajectories near the surface of the asteroid Ryugu, showing possible trajectories and the locating positions of the object on asteroid's surface. Applications of this method are finally discussed, especially for simulating deployments of the lander on Ryugu, showing a feasible landing scheme.

We survey the landing mechanics of objects near Ruygu with our method employed. Due to the observation, the final positions of the objects were relatively concentrated within a release radius of the 2.5 m in free-motion. The method performed in this study may provide a unique opportunity to understand the ongoing Hayabusa2 mission project. A future work should be organized to optimize the surface model to be applicable to asteroids of any shape with complex geography, and simulate the environment condition under complex parameters. It will improve greatly our knowledge of the in situ exploration on an asteroid, reveal why the lander deviated from the target point, and finally help us find a detailed landing scheme.

Acknowledgments

Y. Yu acknowledges support from the Natural Science Foundation of China (Grants No. 11702009 & No. 11525208). L. Z. Shu acknowledges support from the Natural Science Foundation of China (Grant No. 11603057). J. Lv acknowledges support from the Natural Science Foundation of China (Grant No. 11572018). The original polyhedral data of this asteroid adopted in this paper are obtained from the NASA Planetary Data System (PDS) at https://pds.nasa.gov/. Specific details of the code developed for this study can be obtained by contacting the corresponding author.

References

Baxansky, A., & Kiryati, N. (2007). Calculating geometric properties of three-dimensional objects from the spherical harmonic representation. *Pattern recognition*, 40(2), 756-770. doi: 10.1016/j.patcog.2006.06.001

Chapman, C. R. (2004). Space weathering of asteroid surfaces. *Annual Review of Earth and Planetary Sciences*, 32, 539-567. doi: 10.1146/annurev.earth.32.101802.120453

Cheng, A. F., Santo, A. G., Heeres, K. J., Landshof, J. A., Farquhar, R. W., Gold, R. E., & Lee, S.

C. (1997). Near-Earth asteroid rendezvous: Mission overview. *Journal of Geophysical Research: Planets*, 102(E10), 23695-23708. doi: 10.1007/978-94-011-5200-6_1

Ďurech, J., Carry, B., Delbo, M., Kaasalainen, M., & Viikinkoski, M. (2015). Asteroid models from multiple data sources. In Michel, P., Demeo, F. E., & Bottke, W. F., *Asteroids IV* (pp. 183-202). Tucson: University of Arizona. doi: 10.2458/azu_uapress_9780816532131-ch010

Farquhar, R., Kawaguchi, J. I., Russell, C., Schwehm, G., Veverka, J., & Yeomans, D. (2002). Spacecraft exploration of asteroids: The 2001 perspective. In Bottke JR, W. F., Cellino, A., Paolicchi, P., & Binzel, R. P., *Asteroids III* (pp. 367-376). Tucson: University of Arizona.

Fujiwara, A., Kawaguchi, J., Yeomans, D. K., Abe, M., Mukai, T., Okada, T., et al. (2006). The rubble-pile asteroid Itokawa as observed by Hayabusa. *Science*, 312(5778), 1330-1334. doi: 10.1126/science.1125841

Hamilton, D. P., & Burns, J. A. (1992). Orbital stability zones about asteroids: ii. the destabilizing effects of eccentric orbits and of solar radiation. *Icarus*, 96(1), 43-64. doi: 10.1016/0019-1035(92)90005-r

Housen, K. R., & Wilkening, L. L. (1982). Regoliths on small bodies in the solar system. *Annual Review of Earth and Planetary Sciences*, 10(1), 355-376. doi: 10.1146/annurev.ea.10.050182.002035

Housen, K. R., Wilkening, L. L., Chapman, C. R., & Greenberg, R. (1979). Asteroidal regoliths. *Icarus*, 39(3), 317-351. doi: 10.1016/0019-1035(79)90145-3

Hu, Z. W., & Xu, W. B. (2008). *Planetary science*. Science, Beijing.

Li, J. F., & Zeng, X. Y. (2008). Flight dynamics in the gravitional field of irregular asteroids. Advances in Mechanics, 47, 429-451. doi: 10.6052/1000-0992-16-042

Müller, T. G., Ďurech, J., Ishiguro, M., Mueller, M., Krühler, T., Yang, H., et al. (2017). Hayabusa-2 mission target asteroid 162173 Ryugu (1999 JU3): Searching for the object's spin-axis orientation. *Astronomy & Astrophysics*, **599**, A103. doi: 10.1051/0004-6361/201629134

Ostro, S. J., Hudson, R. S., Benner, L. A., Giorgini, J. D., Magri, C., Margot, J. L., & Nolan, M. C. (2002). Asteroid radar astronomy. In Bottke JR, W. F., Cellino, A., Paolicchi, P., & Binzel, R. P., *Asteroids III* (pp. 151-168). Tucson: University of Arizona. doi: 10.1029/RG021i002p00186

Pravec, P., Harris, A. W., & Michalowski, T. (2002). Asteroid rotations. In Bottke JR, W. F., Cellino, A., Paolicchi, P., & Binzel, R. P., *Asteroids III* (pp. 113-122). Tucson: University of Arizona.

Richardson, D. C., Leinhardt, Z. M., Melosh, H. J., Bottke Jr, W. F., & Asphaug, E. (2002). Gravitational aggregates: evidence and evolution. In Bottke JR, W. F., Cellino, A., Paolicchi, P., & Binzel, R. P., *Asteroids III* (pp. 501-515). Tucson: University of Arizona.

Scheeres, D. J., Ostro, S. J., Hudson, R. S., DeJong, E. M., & Suzuki, S. (1998). Dynamics of orbits close to asteroid 4179 Toutatis. *Icarus*, *132*(1), 53-79. doi: 10.1006/icar.1997.5870

Shen, L., & Chung, M. K. (2007). *Large-scale modeling of parametric surfaces using spherical harmonics*. Paper presented at Third International Symposium on 3D Data Processing, Visualization, and Transmission, New York, Ameraca. doi: 10.1109/3DPVT.2006.86

Shen, L., & Makedon, F. (2006). Spherical mapping for processing of 3D closed surfaces. *Image and vision computing*, 24(7), 743-761. doi: 10.1016/j.imavis.2006.01.011

Tardivel, S., Scheeres, D. J., Michel, P., Van wal, S., & Sánchez, P. (2014). Contact motion on surface of asteroid. *Journal of Spacecraft and Rockets*, 51(6), 1857-1871. doi: 10.2514/1.A32939

Tsoulis, D., & Petrović, S. (2001). On the singularities of the gravity field of a homogeneous polyhedral body. *Geophysics*, 66(2), 535-539. doi: 10.1190/1.1444944

Tsuchiyama, A., Uesugi, M., Matsushima, T., Michikami, T., Kadono, T., Nakamura, T., et al. (2011). Three-dimensional structure of Hayabusa samples: origin and evolution of Itokawa regolith. *Science*, 333(6046), 1125-1128. doi: 10.1126/science.1207807

Van Wal, S., & Scheeres, D. J. (2016). The lift-off velocity on the surface of an arbitrary body. *Celestial Mechanics and Dynamical Astronomy*, 125(1), 1-31. doi: 10.1007/s10569-016-9671-6

Van Wal, S., & Scheeres, D. J. (2017). Lift-Off Velocity on Solar-System Small Bodies. *Journal of Guidance, Control, and Dynamics*, 40(8), 1990-2005. doi: 10.2514/1.G002337

Van wal, S., Reid, R., & Scheeres, D. (2017). Small-Body Lander Simulations Using the GPU. *Trans. JSASS Aerospace Tech. Japan*, 14(31).

Wang, S., Yu, Y., & LV, J. (2019). *Large-scale modeling of parametric asteroid surfaces using polynomial series*. SCIENTIA SINICA Physica, Mechanica & Astronomica, 49(8): 084507. 84507(2019). doi: 10.1360/SSPMA-2019-0011

Watanabe, S., Hirabayashi, M., Hirata, N., Hirata, N., Noguchi, R., Shimaki, Y., et al. (2019). Hayabusa2 arrives at the carbonaceous asteroid 162173 Ryugu—A spinning top–shaped rubble pile. *Science*, 364(6437), 268-272. doi: 10.1126/science.aav8032

Werner, R. A., & Scheeres, D. J. (1996). Exterior gravitation of a polyhedron derived and compared with harmonic and mascon gravitation representations of asteroid 4769 Castalia. *Celestial Mechanics and Dynamical Astronomy*, 65(3), 313-344. doi: 10.1007/BF00053511

Yu, Y., & Baoyin, H. (2015). Modeling of migrating grains on asteroid's surface. *Astrophysics and Space Science*, 355(1), 43-56. doi: 10.1007/s10509-014-2140-3

Supporting Information

MOVIE1.avi

MOVIE1.avi indicates the simulation of a deployment on Ryugu with released radius of 2.5m and initial velocity of 0m/s. The blue cloud indicates the objects' initial position, the red cloud indicates the final landing site.

MOVIE2.avi

MOVIE2.avi indicates the simulation of a deployment on Ryugu with released radius of 5m and initial velocity of 0m/s. The blue cloud indicates the objects' initial position, the red cloud indicates the final landing site.

MOVIE3.avi

MOVIE1.avi indicates the simulation of a deployment on Ryugu with released radius of 7m and initial velocity of 0m/s. The blue cloud indicates the objects' initial position, the red cloud indicates the final landing site.

MOVIE4.avi

MOVIE1.avi indicates the simulation of a deployment on Ryugu with released radius of 5m and initial velocity of 1m/s. The blue cloud indicates the objects' initial position, the red cloud indicates the final landing site.

MOVIE5.avi

MOVIE1.avi indicates the simulation of a deployment on Ryugu with released radius of 5m and initial velocity of 1.5m/s. The blue cloud indicates the objects' initial position, the red cloud indicates the final landing site.